Research Article Vol. 30, No. 15 / 18 Jul 2022 / Optics Express 27285

Optics EXPRESS

Narrow bandgap $Al_{0.15}In_{0.85}As_{0.77}Sb_{0.23}$ for mid-infrared photodetectors

ADAM A. DADEY,[1] ANDREW H. JONES,[1] ANDREW J. MCARTHUR,[2] ELLIE Y. WANG,[2] AARON J. MUHOWSKI,[2] SETH R. BANK,[2] AND JOE C. CAMPBELL[1,*]

[1] *Department of Electrical and Computer Engineering, University of Virginia, Charlottesville, Virginia 22903, USA*
[2] *Department of Electrical and Computer Engineering, University of Texas, Austin, Texas 78758, USA*
[*] *jcc7s@virginia.edu*

Abstract: Mid-IR is a useful wavelength range for both science and military applications due to its low atmospheric attenuation and ability to be used for passive detection. However, many solutions for detecting light in this spectral region need to be operated at cryogenic temperatures as their required narrow bandgaps suffer from carrier recombination and band-to-band tunneling at room temperature leading to high dark currents. These problems can be alleviated by using a separate absorption, charge, and multiplication avalanche photodiode. We have recently demonstrated such a device with a 3-µm cutoff using $Al_{0.15}In_{0.85}As_{0.77}Sb_{0.23}$, as the absorber, grown on GaSb. Here we investigate $Al_{0.15}In_{0.85}As_{0.77}Sb_{0.23}$ as a simple PIN homojunction and provide metrics to aid in future designs using this material. PL spectrum measurements indicate a bandgap of 2.94 µm at 300 K. External quantum efficiencies of 39% and 33% are achieved at 1.55 µm and 2 µm respectively. Between 180 K and 280 K the activation energy is ~0.22 eV, roughly half the bandgap of $Al_{0.15}In_{0.85}As_{0.77}Sb_{0.23}$, indicating thermal generation is dominant.

© 2022 Optica Publishing Group under the terms of the Optica Open Access Publishing Agreement

1. Introduction

Mid-wavelength infrared (mid-IR) is a spectral range generally defined as 2- to 5-µm light and is useful for both science and military applications. Low atmospheric attenuation in this optical window is useful for astronomy and infrared imaging. It is also well suited for thermal detection, which is beneficial for night vision systems [1]. Three materials systems are common for mid-IR detection InAs [2], InSb [3], and HgCdTe [4]. By taking advantage of the process of impact ionization, APDs realized in these materials can achieve higher sensitivity than typical photodiodes. However, since these materials systems all have narrow bandgaps, they exhibit high dark currents at room temperature due to carrier recombination and as a result are typically operated at cryogenic temperatures to limit the effect. This limitation is inconvenient for certain applications as cryogenic coolers are complex and bulky. Additionally, the narrow bandgap leads to the onset of band-to-band tunneling at low electric fields. Although, this problem can be alleviated by growing thick structures to reduce the electric field, the dark current with typically suffer as a result.

The use of separate absorption, charge, and multiplication (SACM) structures, which decouple absorption and multiplication, has been successful in reducing the carrier recombination and band-to-band tunneling components of dark current in APDs. This design enables low electric fields in the absorber, limiting tunneling, and high electric fields in the multiplier to promote impact ionization. Recently, we have demonstrated an SACM APD with a cutoff of 3 µm [5] using the $Al_{1-x}In_xAs_{1-y}Sb_y$/GaSb digital alloy materials system. By varying the Al concentration, the bandgap energy of this material can be tuned for detection from the visible to ~5 µm while maintaining a lattice match to the GaSb substrate. This materials system is direct bandgap up to an Al concentration of ~80% [6]. APDs made in this materials system have

#461854 https://doi.org/10.1364/OE.461854
Journal © 2022 Received 20 Apr 2022; revised 25 Jun 2022; accepted 27 Jun 2022; published 13 Jul 2022

Optics EXPRESS

demonstrated high gain and low excess noise [7–10], comparable to that of Si APDs. We have also demonstrated nBn photodetectors operating at 2 µm using $Al_{0.30}In_{0.70}As_{0.67}Sb_{0.33}$ [11,12], and 3 µm using $Al_{0.15}In_{0.85}As_{0.77}Sb_{0.23}$ [13]. The aforementioned 3-µm cutoff SACM also uses $Al_{0.15}In_{0.85}As_{0.77}Sb_{0.23}$ as the absorber. Here, we report material characteristics and device characteristics of $Al_{0.15}In_{0.85}As_{0.77}Sb_{0.23}$ that may be found useful for future photodetector designs incorporating the material for operation in the mid-IR. Material characteristics presented include refractive index, extinction coefficient, absorption coefficient, and the photoluminescence (PL) spectrum. Device characteristics of $Al_{0.15}In_{0.85}As_{0.77}Sb_{0.23}$ PIN photodiodes presented include current-voltage, capacitance-voltage, dark current density versus temperature, responsivity, activation energy, and ideality factor.

2. Growth and fabrication

$Al_{0.15}In_{0.85}As_{0.77}Sb_{0.23}$ PIN epitaxial layers were grown as a digital alloy on an n-type GaSb substrate via molecular beam epitaxy as described previously [6]. Figure 1(a) shows a schematic cross-section of the device. Figure 1(b) shows an X-ray diffraction pattern of the grown with the substrate and superlattice fringe peaks labeled. Figure 2 shows the photoluminescence of the crystal measured at several temperatures. At 78 K the peak is at 2.89 µm with a full width at half maximum of 45 meV (6.7 kT). At 300 K the peak is at 2.94 µm with a full width at half maximum of 81 meV (3.1 kT). The peak at 300 K falls between previously reported PL intensity peaks for $Al_{0.09}In_{0.91}As_{0.31}Sb_{0.69}$ (3.35 µm) and $Al_{0.19}In_{0.81}As_{0.33}Sb_{0.67}$ (2.64 µm) [6]. We suspect the bump present in the PL spectrum around 3.25 µm is due to atmospheric absorption. Ellipsometry was performed with a J.A. Woollam VASE Ellipsometer on the bare epitaxy prior to device fabrication. The wavelength range extended from 280 to 2450 nm with measurement angles from 65° to 75° in 5° increments. Figure 3(a) shows the measured Ψ and Δ at the three angles and their corresponding fits obtained using a B-spline fitting approach. Refractive indices, extinction coefficients, and absorption coefficients were extracted from the fits and are displayed in Fig. 3(b).

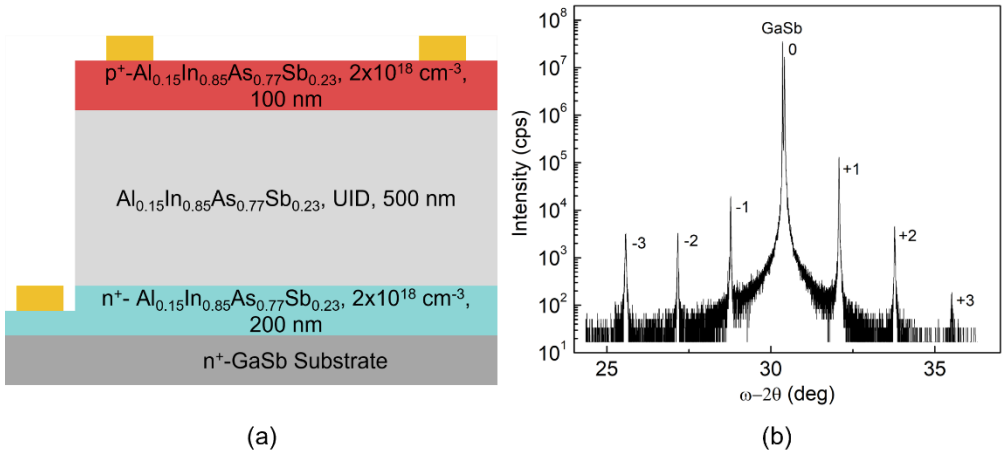

Fig. 1. (a) The schematic device cross-section for an $Al_{0.15}In_{0.85}As_{0.77}Sb_{0.23}$ PIN, (b) the X-ray diffraction pattern for $Al_{0.15}In_{0.85}As_{0.77}Sb_{0.23}$/GaSb.

Following epitaxial characterization, circular mesas were defined using standard lithography techniques and were wet etched using a solution of $C_6H_8O_7$:H_3PO_4:H_2O_2:H_2O (10 g:6 mL:3 mL:60 mL). After forming the mesas, Ti/Au (10 nm/100 nm) contacts were deposited via e-beam evaporation on both the p- and n-contact layers.

Optics EXPRESS

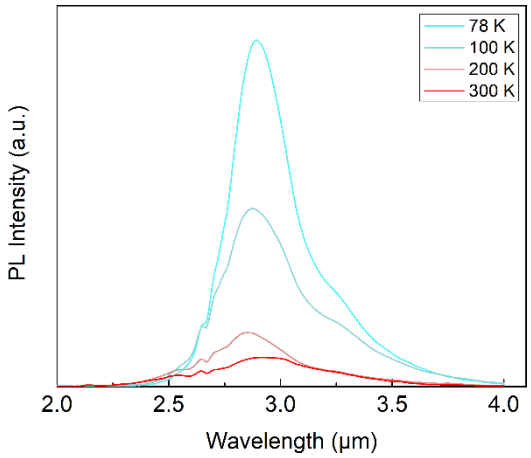

Fig. 2. The photoluminescence versus wavelength for $Al_{0.15}In_{0.85}As_{0.77}Sb_{0.23}$/GaSb at different temperatures.

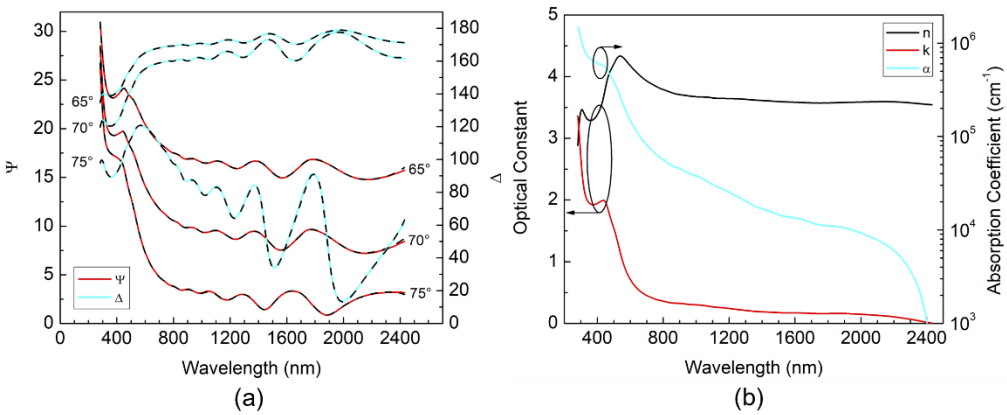

Fig. 3. (a) Measured Ψ (left axis) and Δ (right axis) with their corresponding fits (dashed), and (b) the extracted refractive indices, extinction coefficients (left axis), and absorption coefficients (right axis) for $Al_{0.15}In_{0.85}As_{0.77}Sb_{0.23}$/GaSb.

Optics EXPRESS

3. Device characterization

Current-voltage curves were measured with an HP 4145 Semiconductor Parameter Analyzer in a cryogenic chamber cooled with liquid nitrogen. Figure 4(a) shows the dark current and photocurrent obtained using a temperature-stabilized 2-µm fiber-coupled laser diode at 200 K. For the photocurrent curve, ~27 µW of light was incident on the top of the mesa. The light was focused with a fiber lens to a spot size smaller than the mesa diameter to ensure no sidewall illumination. A characteristic kink in the dark current curve is visible at -4.5 V, indicating the onset of tunneling. The photocurrent is constant out to the intersection of the photocurrent and dark current curves. Figure 4(b) shows the capacitance-voltage curve for a 200-µm-diameter device measured with an HP 3275A LCR meter at room temperature under blackout conditions. At a reverse bias of 2 V, the capacitance has leveled off, indicating the device is fully depleted. Dark current was measured in 20-K increments from 100 K to 300 K and is plotted as dark current density in Fig. 5(a). Figure 5(b) shows the dark current, under a -2 V bias at 300 K, for devices of different mesa sizes plotted against mesa diameter. The quadratic fit indicates the dark current is bulk-limited. The quadratic fit holds up until the onset of band-to-band tunneling at -5 V. Responsivity was measured at 300 K at 1.55 µm and 2 µm with temperature-stabilized fiber-coupled laser diode illumination. A reverse bias of 2 V was used to ensure full depletion of the device. At 1.55 µm and 2 µm the responsivity was 0.49 A/W and 0.53 A/W respectively, corresponding to external quantum efficiencies of 39% and 33% respectively. The theoretical external quantum efficiency, η, can be calculated with $\eta = (1\text{-}R)(\exp(-\alpha W))$, where R is the surface reflection, α is the absorption coefficient, and W is the depletion width (500 nm). Using the refractive index and absorption coefficient in Fig. 3(b) at 1.55 µm and 2 µm the theoretical external quantum efficiencies are 35% and 25% respectively. The difference between the theoretical and measured quantum efficiencies is likely due to uncertainty with fitting the optical constants. We used a B-spline approach for fitting as there is no reference model for $Al_{1-x}In_xAs_{1-y}Sb$. We also note that the depletion region is only 500-nm thick and there is no anti-reflection coating. From the optical constants in Fig. 3(b) we can calculate a normal incidence surface reflection at 1.55 µm and 2 µm of ~31%. Therefore, with a proper 1%-reflectivity anti-reflection coating we can expect quantum efficiencies up to ~57% and ~48% at 1.55-µm and 2-µm illumination respectively.

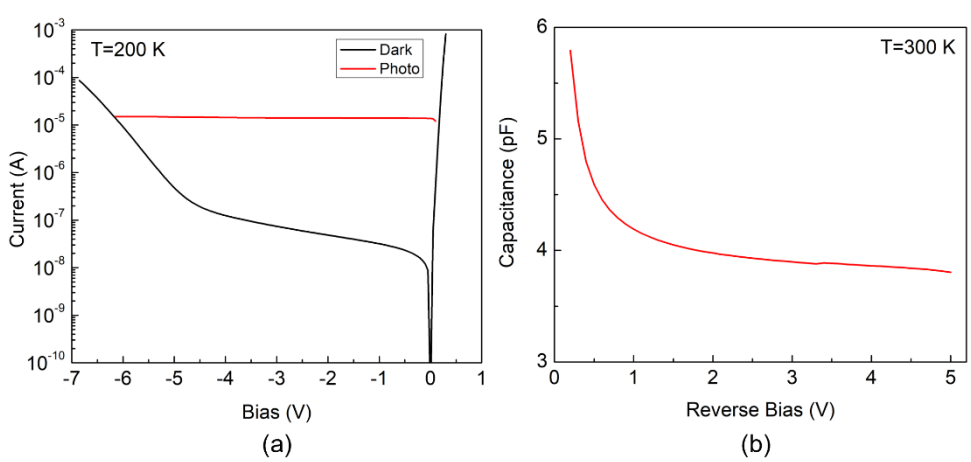

Fig. 4. (a) Current-voltage characteristic at 200 K for a 150-µm-diameter $Al_{0.15}In_{0.85}As_{0.77}Sb_{0.23}$ PIN with photocurrent, under ~27 µW of 2-µm illumination, and dark current. (b) A capacitance-voltage curve at 300 K for a 200-µm-diameter device.

Optics EXPRESS

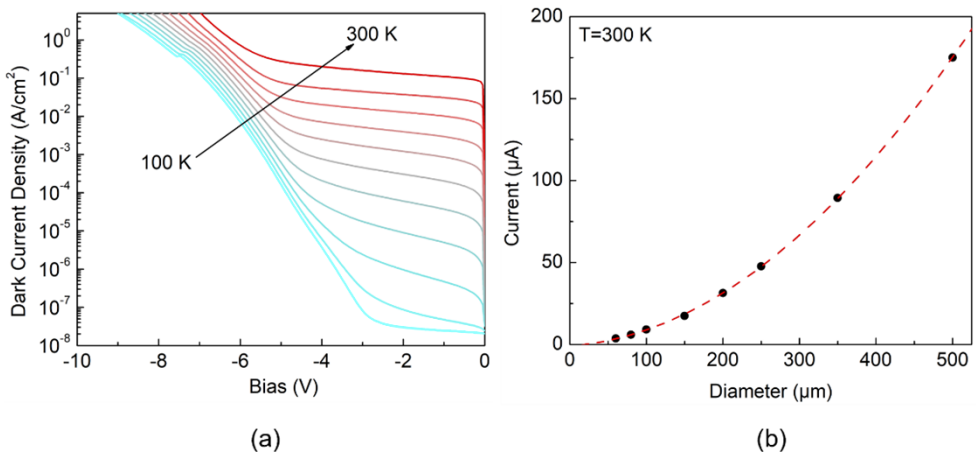

Fig. 5. (a) Dark current density versus temperature curves from 100 K to 300 K in 20-K increments, and (b) dark current versus diameter curve with a corresponding quadratic fit at 300 K.

The activation energy was extracted from the measurements in Fig. 5(a) using the relation,

$$I_{dark} \propto T^2 \exp\left(\frac{-E_a}{k_B T}\right) \tag{1}$$

where I_{dark} is the measured dark current, T is the temperature in kelvin, E_a is activation energy, and k_B is the Boltzmann constant. Figure 6 shows dark current density plotted against inverse temperature for reverse bias voltages from 1 V to 5 V in 1-V increments for a 150-μm-diameter device. Equation (1) was used to fit curves to the measured values and extract an activation energy for each bias voltage. The extracted activation energies are plotted in the inset. The bandgap for $Al_{0.15}In_{0.85}As_{0.77}Sb_{0.23}$ is known to be ~0.4 eV [6]. These activation energies are approximately half the bandgap energy, which indicates that thermal generation dominates. At low temperatures under 4 V and 5 V reverse bias, the activation energy is likely dominated by trap-assisted tunneling current [14].

The forward current-voltage characteristic was measured from 200 K to 380 K in 20-K increments using a Keithley 2400 SourceMeter. At each temperature, the measured curve was fit with Eq. (2) to extract the ideality factor. J is the measured forward current density, J_S is the reverse saturation current density, q is the elementary charge, V is the applied voltage, n is the ideality factor, k_B is the Boltzmann constant, and T is the temperature in kelvin.

$$J = J_S\left(\exp\left(\frac{qV}{nk_B T}\right) - 1\right) \tag{2}$$

Both J_S and n were fit to the measured data using Eq. (2). Figure 7(a) shows the measured forward current density for a 200-μm-diameter device with fits shown as dashed lines. There is excellent agreement between the measured data and the fit curves. Figure 7(b) shows the extracted ideality factor plotted against temperature for two different mesa diameters, 150 μm and 200 μm. Two different size devices were measured to assess the role of surface effects. From 200 K to 300 K the ideality factors for the two sizes are the same and decrease with increasing temperature. This inverse trend between ideality factor and temperature has been previously reported in other structures [15,16]. However, above 300 K, the ideality factor increases with temperature and the two mesa diameters diverge. The sharp increase in ideality factor above 300

Optics EXPRESS

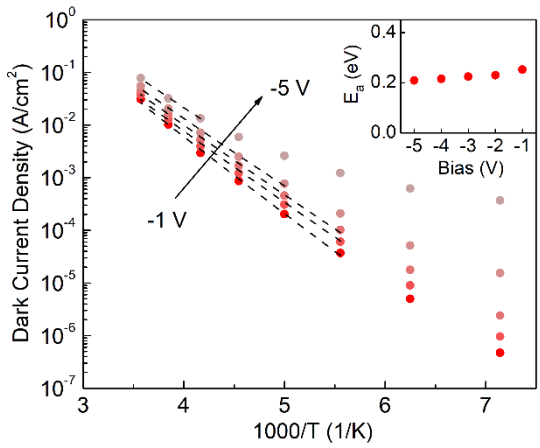

Fig. 6. Dark current density versus inverse temperature for the $Al_{0.15}In_{0.85}As_{0.77}Sb_{0.23}$ PIN from -1 V to -5 V in 1-V increments with Eq. (1) fits (dashed). The inset shows the extracted activation energy versus bias.

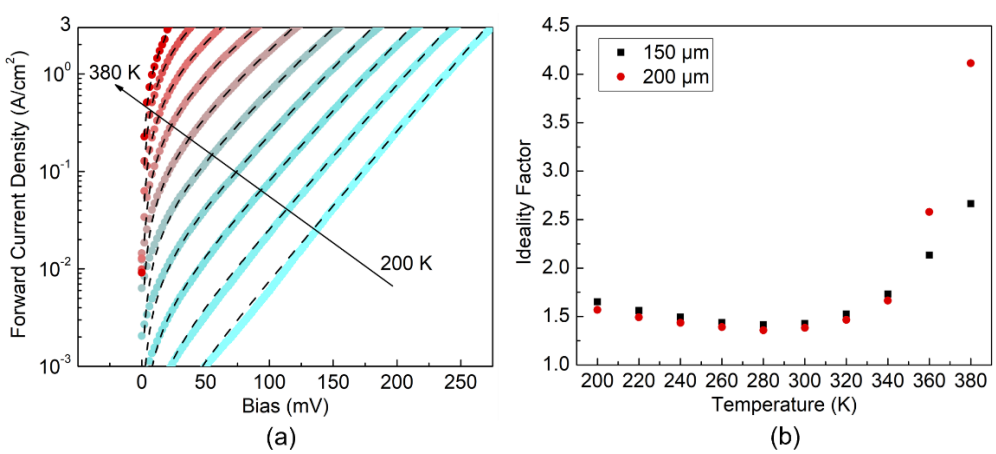

Fig. 7. (a) Forward current density versus bias for the $Al_{0.15}In_{0.85}As_{0.77}Sb_{0.23}$ PIN from 200 K to 380 K in 20-K increments with Eq. (2) fits (dashed), and (b) the extracted ideality factor versus temperature for a 150-μm-diameter device (square) and a 200-μm-diameter device (circle).

Optics EXPRESS

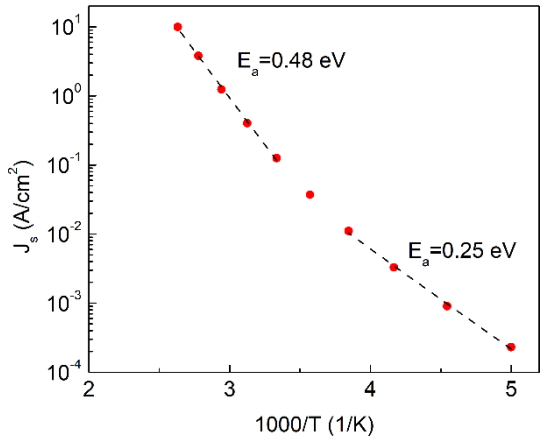

Fig. 8. Reverse saturation current density, J_s, versus inverse temperature for the $Al_{0.15}In_{0.85}As_{0.77}Sb_{0.23}$ PIN with the corresponding activation energy fit using (1).

K likely results from the activation of surface effects, as indicated by the greater increase of the 200-µm-diameter device compared to the 150-µm-diameter device.

The fit J_s is plotted versus inverse temperature in Fig. 8. Using the fit J_s the activation energy was extracted using a similar method as used in Fig. 6. Under a similar temperature range as above the activation energy is 0.25 eV, similar to values above. At higher temperatures, above 300 K, the extracted activation energy is 0.48 eV. This activation energy is similar to the bandgap of $Al_{0.15}In_{0.85}As_{0.77}Sb_{0.23}$ indicating diffusion current dominates.

4. Conclusion

We have reported several material characteristics of $Al_{0.15}In_{0.85}As_{0.77}Sb_{0.23}$/GaSb. Refractive indices, extinction coefficients and absorption coefficients are presented along with a PL spectrum peaking at 2.94 µm at 300 K. Device parameters for $Al_{0.15}In_{0.85}As_{0.77}Sb_{0.23}$ PIN photodiodes are also presented. Dark current versus diameter measurements indicate the dark current of the fabricated PIN photodiodes is bulk-limited. External quantum efficiencies of 39% and 33% are achieved at 1.55 µm and 2 µm respectively. Extracted from the reverse dark current density, the activation energy between 180 K and 280 K is ~0.22 eV, around half the bandgap energy of $Al_{0.15}In_{0.85}As_{0.77}Sb_{0.23}$, indicating thermal generation is dominant. Ideality factor is plotted versus temperature for two different mesa diameters. Between 200 K and 300 K the ideality factors decrease with increasing temperature. Above 300 K, the sharp increase in ideality factor and divergence between the two mesa diameters is likely caused by the activation of surface effects. These results may be useful in future photodetector designs using $Al_{0.15}In_{0.85}As_{0.77}Sb_{0.23}$ for operation in mid-IR.

Funding. Defense Advanced Research Projects Agency (W909MY-12-D-0008); Army Research Office (W911NF-17-1-0065).

Disclosures. The authors declare no conflicts of interest.

Data availability. Data underlying the results presented in this paper are not publicly available at this time but may be obtained from the authors upon reasonable request.

References

1. M. Razeghi and B.-M. Nguyen, "Advances in mid-infrared detection and imaging: a key issues review," Rep. Prog. Phys. **77**(8), 082401 (2014).
2. W. Sun, Z. Lu, X. Zheng, J. C. Campbell, S. J. Maddox, H. P. Nair, and S. R. Bank, "High-Gain InAs Avalanche Photodiodes," IEEE J. Quantum Electron. **49**(2), 154–161 (2013).

Optics EXPRESS

3. J. Abautret, J. P. Perez, A. Evirgen, J. Rothman, A. Cordat, and P. Christol, "Characterization of midwave infrared InSb avalanche photodiode," J. Appl. Phys. **117**(24), 244502 (2015).
4. O. Gravrand, J. Rothman, C. Cervera, N. Baier, C. Lobre, J. P. Zanatta, O. Boulade, V. Moreau, and B. Fieque, "HgCdTe Detectors for Space and Science Imaging: General Issues and Latest Achievements," J. Electron. Mater. **45**(9), 4532–4541 (2016).
5. A. H. Jones, S. D. March, A. A. Dadey, A. J. Muhowski, S. R. Bank, and J. C. Campbell, "AlInAsSb Separate Absorption, Charge, and Multiplication Avalanche Photodiodes for Mid-Infrared Detection," IEEE J. Quantum Electron. **108**(19), 191108 (2022).
6. S. J. Maddox, S. D. March, and S. R. Bank, "Broadly Tunable AlInAsSb Digital Alloys Grown on GaSb," Cryst. Growth Des. **16**(7), 3582–3586 (2016).
7. M. E. Woodson, M. Ren, S. J. Maddox, Y. Chen, S. R. Bank, and J. C. Campbell, "Low-noise AlInAsSb avalanche photodiode," Appl. Phys. Lett. **108**(8), 081102 (2016).
8. A. H. Jones, S. D. March, S. R. Bank, and J. C. Campbell, "Low-noise high-temperature AlInAsSb/GaSb avalanche photodiodes for 2-µm applications," Nat. Photonics **14**(9), 559–563 (2020).
9. M. Ren, S. Maddox, Y. Chen, M. Woodson, J. C. Campbell, and S. Bank, "AlInAsSb/GaSb staircase avalanche photodiode," Appl. Phys. Lett. **108**(8), 081101 (2016).
10. M. Ren, S. J. Maddox, M. E. Woodson, Y. Chen, S. R. Bank, and J. C. Campbell, "Characteristics of $Al_xIn\ 1-_xAs\ _ySb1-\ _y$ (x:0.3−0.7) Avalanche Photodiodes," J. Lightwave Technol. **35**(12), 2380–2384 (2017).
11. D. Chen, R. Wang, J. Andrew McArthur, X. Xue, A. H. Jones, S. R. Bank, and J. C. Campbell, "Demonstration of infrared nBn photodetectors based on the AlInAsSb digital alloy materials system," Appl. Phys. Lett. **119**(3), 031101 (2021).
12. R. Wang, D. Chen, J. A. McArthur, X. Xue, A. H. Jones, S. R. Bank, and J. C. Campbell, "Al0.3InAsSb/Al0.7InAsSb Digital Alloy nBn Photodetectors," J. Lightwave Technol. **40**(1), 113–120 (2022).
13. R. Wang, J. A. Mcarthur, S. R. Bank, and J. C. Campbell, "Infrared Al lt;sub gt;0.15 lt;/sub gt;InAsSb digital alloy nBn photodetectors," J. Lightwave Technol. 1 (2022).
14. J. Huang, J. Huang, C. Zhao, C. Zhao, B. Nie, B. Nie, S. Xie, S. Xie, D. C. M. Kwan, X. Meng, Y. Zhang, Y. Zhang, D. L. Huffaker, W. Ma, W. Ma, and W. Ma, "High-performance mid-wavelength InAs avalanche photodiode using $AlAs_{0.13}Sb_{0.87}$ as the multiplication layer," Photonics Res. **8**, 755–759 (2020).
15. J. Verschraegen, M. Burgelman, and J. Penndorf, "Temperature dependence of the diode ideality factor in CuInS2-on-Cu-tape solar cells," Thin Solid Films **480-481**, 307–311 (2005).
16. M. K. Hudait and S. B. Krupanidhi, "Doping dependence of the barrier height and ideality factor of Au/n-GaAs Schottky diodes at low temperatures," Phys. B (Amsterdam, Neth.) **307**(1-4), 125–137 (2001).